





Genome-scale metabolic models for natural and long-term drug-induced viral control in HIV infection

Anoop T Ambikan^{1,*}, Sara Svensson-Akusjärvi^{1,*} , Shuba Krishnan¹, Maike Sperk¹, Piotr Nowak^{1,2}, Jan Vesterbacka², Anders Sönnnerborg^{1,2}, Rui Benfeitas³, Ujjwal Neogi^{1,4} 

Genome-scale metabolic models (GSMMs) can provide novel insights into metabolic reprogramming during disease progression and therapeutic interventions. We developed a context-specific system-level GSMM of people living with HIV (PLWH) using global RNA sequencing data from PBMCs with suppressive viremia either by natural (elite controllers, PLWH_{EC}) or drug-induced (PLWH_{ART}) control. This GSMM was compared with HIV-negative controls (HC) to provide a comprehensive systems-level metabo-transcriptomic characterization. Transcriptomic analysis identified up-regulation of oxidative phosphorylation as a characteristic of PLWH_{ART}, differentiating them from PLWH_{EC} with dysregulated complexes I, III, and IV. The flux balance analysis identified altered flux in several intermediates of glycolysis including pyruvate, α -ketoglutarate, and glutamate, among others, in PLWH_{ART}. The in vitro pharmacological inhibition of OXPHOS complexes in a latent lymphocytic cell model (J-Lat 10.6) suggested a role for complex IV in latency reversal and immunosenescence. Furthermore, inhibition of complexes I/III/IV induced apoptosis, collectively indicating their contribution to reservoir dynamics.

DOI 10.26508/lsa.202201405 | Received 11 February 2022 | Revised 2 May 2022 | Accepted 2 May 2022 | Published online 10 May 2022

Introduction

During HIV-1 infection, cellular metabolic activity, combined with glycolytic enzymes, regulates susceptibility to HIV-1 at the cellular level (Clerc et al, 2019; Valle-Casuso et al, 2019). Elevated oxidative phosphorylation (OXPHOS) and glycolysis thus favor infection in CD4⁺ T cells (Clerc et al, 2019; Valle-Casuso et al, 2019). CD4⁺ T cells up-regulate glycolysis to meet the energy-demanding turnover for HIV-1 virion production, resulting in their eventual death (Hegedus et al, 2014; Palmer et al, 2014). After initiation of combination antiretroviral therapy (cART), virus-induced short-term metabolic changes do not restore the transient metabolic modulation caused

by the infection. Altered amino acid (AA) metabolism has been reported in untreated people living with HIV-1 (PLWH) as well as within the first 2 yr after initiation of cART compared with the HIV-negative controls (Cassol et al, 2013; Peltenburg et al, 2018). In our recent extensive multi-omics system biology studies on cohorts from India (Babu et al, 2019; Gelpi et al, 2021), Cameroon (Gelpi et al, 2021), and Denmark (Gelpi et al, 2021; Villumsen et al, 2022), we mapped the in-depth metabolomic dysregulation associated with long-term treatment in PLWH. Our group (Babu et al, 2019; Gelpi et al, 2021; Villumsen et al, 2022), and others (Mukerji et al, 2016; Rosado-Sánchez et al, 2019; Valle-Casuso et al, 2019; Meeder et al, 2021; Shytaj et al, 2021), have highlighted how the coordinated modulation of central carbon metabolism, AA metabolism, glutaminolysis, and fatty acid biosynthesis can potentiate accentuated immune aging and cognitive decline in a subset of PLWH on therapy who have dysregulated metabolic profile.

Elite controllers (EC) are a unique group of PLWH that naturally control viral replication and maintain a low viral reservoir. Our recent study indicated that EC had a distinct lipid profile, reduced inflammation, and increased antioxidant defense which may contribute to the EC status (Akusjärvi et al, 2022). Moreover, the integrative proteomic and transcriptomic analysis suggested that the EC group had a unique metabolic uptake and flux profile through hypoxia-inducible factor signaling and glycolysis, which could contribute to the natural control of HIV-1 infection (Akusjärvi et al, 2022). A study also showed how suboptimal inhibition of glycolysis in CD4⁺ T cells decreased the latently infected reservoir (Valle-Casuso et al, 2019). However, EC is heterogeneous, and one mechanism of elite control does not exist (Zhang et al, 2018; Akusjärvi et al, 2022). Instead, PLWH on long-term successful therapy with prolonged suppressive viremia are more homogenous in their immune profile (Zhang et al, 2017). A deep understanding of the immune profile of these groups of HIV-1-infected individuals could help to develop strategies for analytical treatment interventions (ATI) to achieve a clinically relevant ART-free HIV cure or remission (Julg et al, 2019).

¹Division of Clinical Microbiology, Department of Laboratory Medicine, Karolinska Institutet, ANA Futura, Campus Flemingsberg, Stockholm, Sweden ²Department of Medicine, Huddinge (MedH), Karolinska Institutet, ANA Futura, Campus Flemingsberg, Stockholm, Sweden ³National Bioinformatics Infrastructure Sweden (NBIS), Science for Life Laboratory, Department of Biochemistry and Biophysics, Stockholm University, Stockholm, Sweden ⁴Manipal Institute of Virology (MIV), Manipal Academy of Higher Education, Manipal, Karnataka, India

Correspondence: ujjwal.neogi@ki.se

*Anoop T Ambikan and Sara Svensson-Akusjärvi contributed equally to this work.

Genome-scale metabolic models (GSMMs) can provide novel insights toward understanding host–pathogen interactions and metabolic reprogramming during acute and chronic infections. When applied to PBMCs, GSMM can contribute to unraveling the mechanistic processes at the systems level (Ambikan et al, 2022). By combining contextualized PBMC-specific biological network analysis, GSMMs, and multi-omics integration, one can attain holistic and dynamic characterizations of complex rearrangements during disease progression or therapeutic interventions (Yang et al, 2021; Zeybel et al, 2021).

In the present study, we sought to understand and infer changes in HIV-1 infection at the system level by comparing successfully treated PLWH on prolonged cART (herein PLWH_{ART}) with the HIV-seropositive ECs (herein PLWH_{EC}) and HIV-negative controls (herein HC). Contextualized PBMC-specific GSMMs and biological networks were thus developed for PLWH_{ART} and PLWH_{EC} to identify the metabolic alterations during prolonged therapy. We further modulated the key pathways pharmacologically to determine their role in HIV-1 reservoir dynamics and immune senescence profile. By combining the multi-dimensional omics data, our study is the first to provide a comprehensive mapping of the immunometabolic dysregulations using GSMM in PLWH_{ART} with successful long-term treatment. Furthermore, our comparative analysis with PLWH_{EC} offers mechanistic insights into natural immune control.

Results

Clinical characteristics

The study population included three PLWH cohorts, where two groups had suppressed viremia (PLWH_{ART} and PLWH_{EC}, $n = 19$ each), and one untreated group was viremic (herein PLWH_{VP}, $n = 19$). In addition, we included 19 HC. Given that extensive transient metabolic changes occur in the PLWH_{VP} due to the acute viremic phase, we used this group to develop the cART-specific model only (see the Materials and Methods section). The clinical characteristics are given in Table S1. The median (IQR) duration of diagnosed HIV-1 seropositivity infection for PLWH_{EC} was 9 (5–14) yr, and none had received treatment. In PLWH_{ART}, the median duration of suppressive therapy was 13 (7–17) yr with no viral blips except for two individuals. At the time of sample collection, both PLWH_{ART} and PLWH_{EC} had undetectable plasma viral load (<20 copies/ml) and CD4⁺ T-cell counts (>500 cells/ μ l) indicative of significant immune reconstitution.

System-level PBMC-based gene expression identifies dysregulation of OXPHOS in PLWH_{ART}

To identify the system-level host response during HIV-1 infection, we performed transcriptomic profiling of total RNA isolated from PBMCs. The differential gene expression analysis was performed between all pair-wise comparisons among the four groups (adjusted $P < 0.05$, Supplemental Data 1). No genes were found to be dysregulated between PLWH_{EC} and HC, whereas 949 genes were differentially expressed between PLWH_{ART} and HC (adjusted $P < 0.05$). To identify whether the changes in gene expression between

the groups were due to the altered cell-type proportions, we performed digital cell quantification (DCQ), estimating cell-type proportions in each group (Racle & Gfeller, 2020). We characterized 18 immune cell populations (Figs 1A and S1). As expected, the proportion of several cell types was significantly different in PLWH_{VP} compared with the other groups. No significant difference in the proportion of cell types was observed between PLWH_{EC} and HC and the only difference in regulatory T cells (Tregs) was observed between PLWH_{EC} and PLWH_{ART} ($P < 0.05$). Based on the differentially expressed genes, we identified 1,037 specifically dysregulated genes in PLWH_{ART} (see the Materials and Methods section) with an explicitly differential regulation in PLWH_{ART} (Supplemental Data 2). Sample clustering using the cART-specific genes separated PLWH_{ART} samples from the other groups (Fig 1B). One PLWH_{ART} sample (marked by an arrow) (Fig 1B) was identified as belonging to a patient who had been classified in the past as an EC but started treatment 23 yr after HIV-1 diagnosis (date of diagnosis: 05 January, 1989, treatment initiation 11 December, 2012) due to two successive viral loads were above the detection limit (240 and 185 copies/ml, respectively). The patient maintained viral load below detection level following treatment. Gene set enrichment analysis (GSEA) using MSigDB hallmark gene sets on the ART-specific genes highlighted that the primary mechanisms related to the long-term treatment were OXPHOS (adjusted $P < 0.05$) and reactive oxygen species (ROS) pathways (adjusted $P < 0.1$), as the top significantly regulated gene sets (Fig 1C).

Larger viral reservoir and up-regulated OXPHOS differentiate PLWH_{ART} from PLWH_{EC}

Next, we performed a comparative analysis between PLWH_{EC} and PLWH_{ART} to identify the immune signature during suppressive viremia that is naturally controlled, or cART induced. First, we performed relative reservoir quantification on total PBMC HIV-1 DNA and observed that PLWH_{ART} had a significantly larger reservoir than PLWH_{EC} (Fig 2A). Furthermore, we performed differential gene expression analysis between PLWH_{EC} and PLWH_{ART} to identify the cART related changes during suppressive viremia. We identified 1,061 significantly dysregulated genes in PLWH_{ART} compared with PLWH_{EC} (adjusted $P < 0.05$). There were 400 genes up-regulated and 661 genes down-regulated in PLWH_{ART} compared with PLWH_{EC} (Fig 2B). The dysregulated genes displayed distinct expression patterns in the two groups and hierarchical clustering, showing apparent clustering of PLWH_{ART} and PLWH_{EC} samples (Fig 2C). No other factors like age, duration of treatment, and gender showed any clustering pattern. The GSEA analysis using the MSigDB hallmark gene set showed that OXPHOS and ROS pathways were significantly enriched with most of the genes up-regulated in PLWH_{ART} (Fig 2D) (false discovery rate [FDR] < 0.2). Pathways with most genes down-regulated in PLWH_{ART} were not statistically significant. Pathways such as mTORC1 signaling and glycolysis also appeared in the analysis, with most of the genes up-regulated in PLWH_{ART} but without passing the significance threshold (FDR > 0.2). OXPHOS was identified as significantly altered in long-term treated patients. Therefore, we looked at OXPHOS in detail to find which complexes were most affected. Among the genes in the five complexes of OXPHOS (I to V), complexes I (34%), III (45%), and IV (45%) were

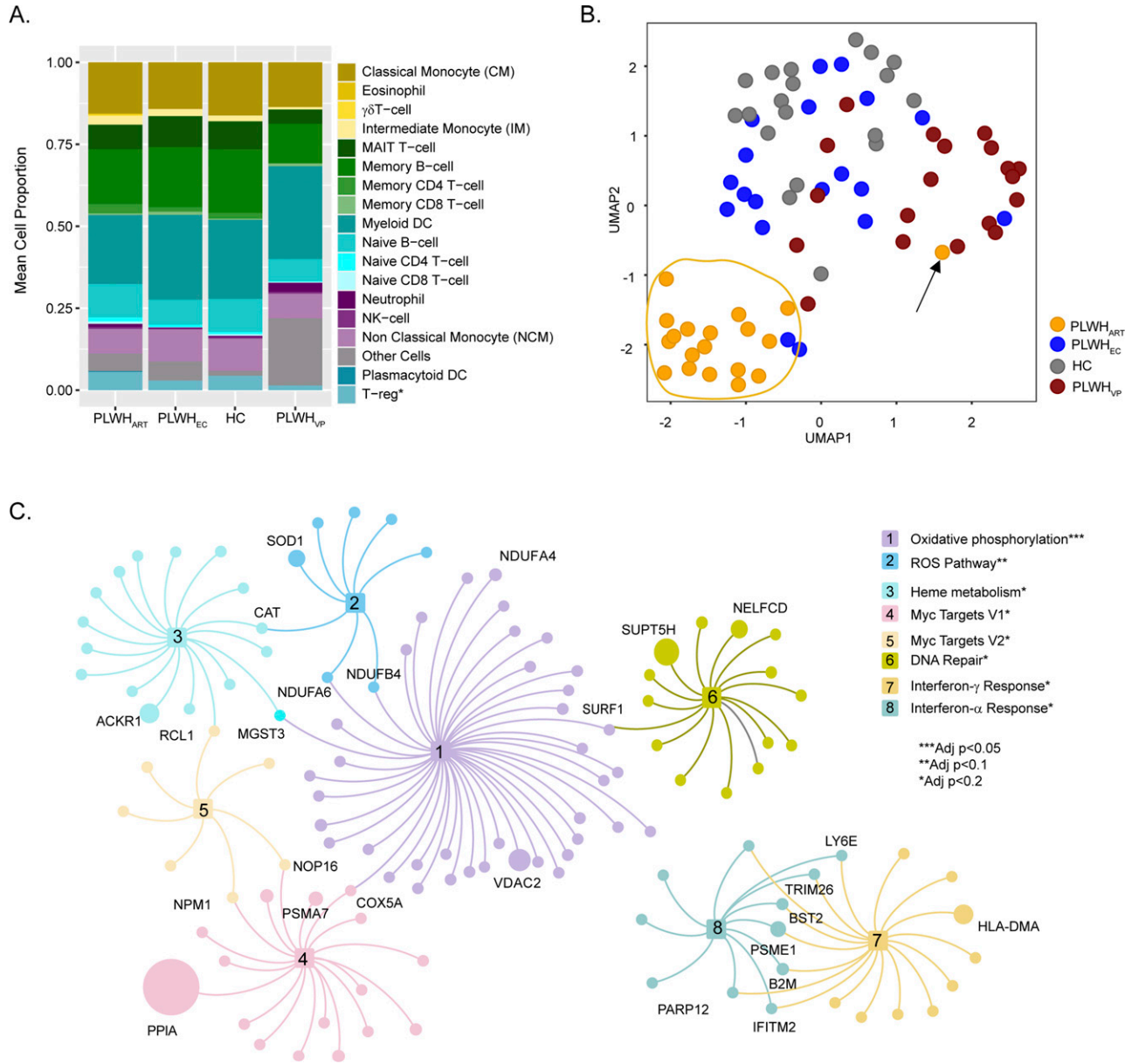


Figure 1. System-level transcriptomics signature in PLWH_{ART}.

(A) Digital cell-type quantification using Estimating the Proportions of Immune and Cancer cell (EPIC) methodology. Mean cell proportions estimated from the samples of each of the four cohorts are visualized in the bar graph. (B) Visualization of sample distribution using expression of combination antiretroviral therapy-specific genes and dimensionality reduction by UMAP. (C) Network visualization of pathways identified as significantly enriched by combination antiretroviral therapy-specific genes. Nodes are genes and edges represent association with pathways. Node size is relative to the mean expression of the genes among the PLWH_{ART}. Genes overlapping between pathways and high abundance genes are labeled.

primarily affected in PLWH_{ART} compared with PLWH_{EC} (Fig 2E). We also checked the overlap between the ART-specific genes (n = 1,037) and the differentially regulated genes between the PLWH_{ART} and PLWH_{EC} (n = 1,061). We observed that 557 genes were overlapping between the two sets of genes. The gene list enrichment analysis using MSigDB hallmark gene set identified OXPPOS (adjusted *P* < 0.001), MYC targets V1 (adjusted *P* = 0.004), and ROS pathway (adjusted *P* = 0.04) as significant pathways. Combining all the data, up-regulation of the OXPPOS was the hallmark of PLWH_{ART} and complexes I, III, and IV were primarily affected.

Altered flux balance in PLWH on cART is linked to OXPPOS, glycolysis, and TCA cycle

Given that significant metabolic pathway-centered perturbations were found in PLWH_{ART}, we next performed reporter metabolite analysis to identify metabolites around which most of the transcriptional changes occurred. Five metabolites, namely, superoxide, ubiquinol, ubiquinone, ferrocytochrome C, and ferricytochrome C were significantly up-regulated in PLWH_{ART} compared with PLWH_{EC} (adjusted *P* < 0.2) (Fig 3A). In addition, nicotinamide adenine

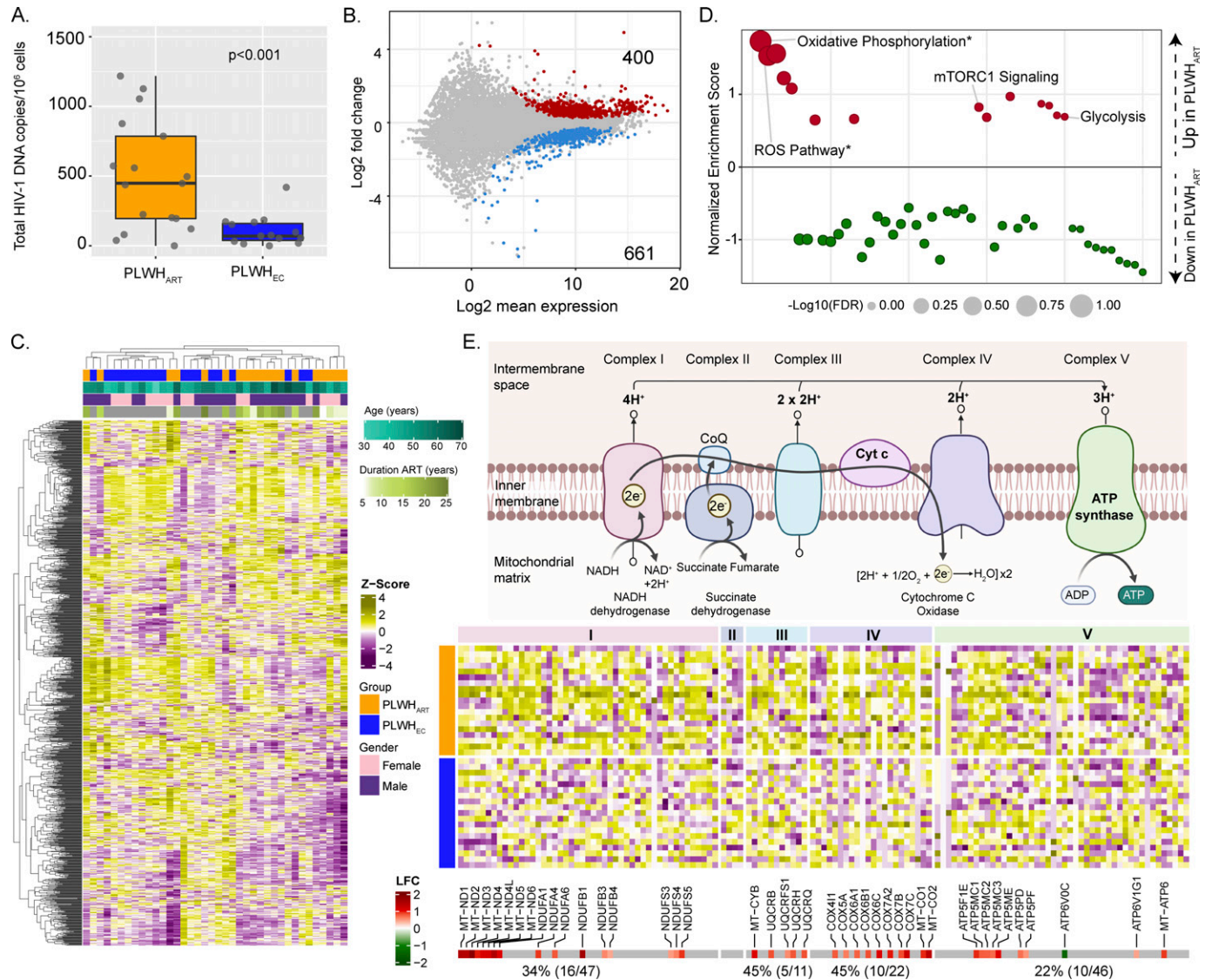


Figure 2. Comparative analysis of PLWH_{ART} and PLWH_{EC}.

(A) Relative reservoir quantification using total HIV-1 DNA in PLWH_{ART} (n = 17) and PLWH_{EC} (n = 14). (B) MA plot showing differential gene expression results of PLWH_{ART} versus PLWH_{EC}. Negative log₂-fold change values represent down-regulation and positive values represent up-regulation in PLWH_{ART}. Grey-colored dots denote non-significant genes (adjusted *P* > 0.05). (C) Heatmap showing the expression pattern of significantly regulated genes between PLWH_{ART} and PLWH_{EC} (adjusted *P* < 0.05). Column annotation denotes cohort, age, gender, and duration of combination antiretroviral therapy of the corresponding samples. Row and column clustering was performed using Euclidian distance. (D) Gene set enrichment analysis results using MSigDB hallmark gene set between PLWH_{ART} versus PLWH_{EC}. A positive enrichment score represents up-regulation and negative score represents down-regulation in PLWH_{ART}. Statistically significant pathways are labeled and highlighted by asterisk. Bubble size is relative to the adjusted *P*-values of the pathways. *Indicates FDR < 0.2. (E) Schematic visualization of the five complexes of OXPHOS pathway. The heatmap shows expression pattern of genes belonging to OXPHOS pathway in PLWH_{ART} and PLWH_{EC}. Column annotation denotes OXPHOS pathway complexes and row annotation denotes the cohort. The bottom annotation shows the log₂ fold change values of the genes. Red color represents up-regulation and green color represents down-regulation of the gene in PLWH_{ART} compared with PLWH_{EC}.

dinucleotide hydrogen, S-adenosyl methionine, and S-adenosyl-L-homocysteine were predicted to be significantly dysregulated in PLWH_{ART} (adjusted *P* < 0.2) (Fig 3A). The overall results suggested a significant change in porphyrin, glycine, serine, and threonine metabolism, and a positive regulation in OXPHOS. The reactions involving significant reporter metabolites, catalyzed by genes in complexes I, III, and IV of OXPHOS (Fig S2), had a distinct expression pattern in PLWH_{ART} compared with PLWH_{EC}. Next, we performed context (disease state)-specific GSMM and flux balance analysis

(FBA) to calculate the metabolic flux in response to transcriptional changes in the PLWH_{ART}, PLWH_{EC}, and HC cohorts (Fig 3B). Context-specific metabolic models for PLWH_{ART}, PLWH_{EC}, and HC having 6,179, 6,237, and 6,199 reactions and 1,799, 1,842, and 1,834 genes/transcripts catalyzing them, respectively, were developed (available: github.com/neogilab/LongART). After excluding the reactions with same directional fluxes in all the three cohorts and reactions with insignificant flux (<10⁻⁵ mmol/h/gDCW), 80 reactions (Supplemental Data 3) were found to be uniquely regulated in PLWH_{ART}

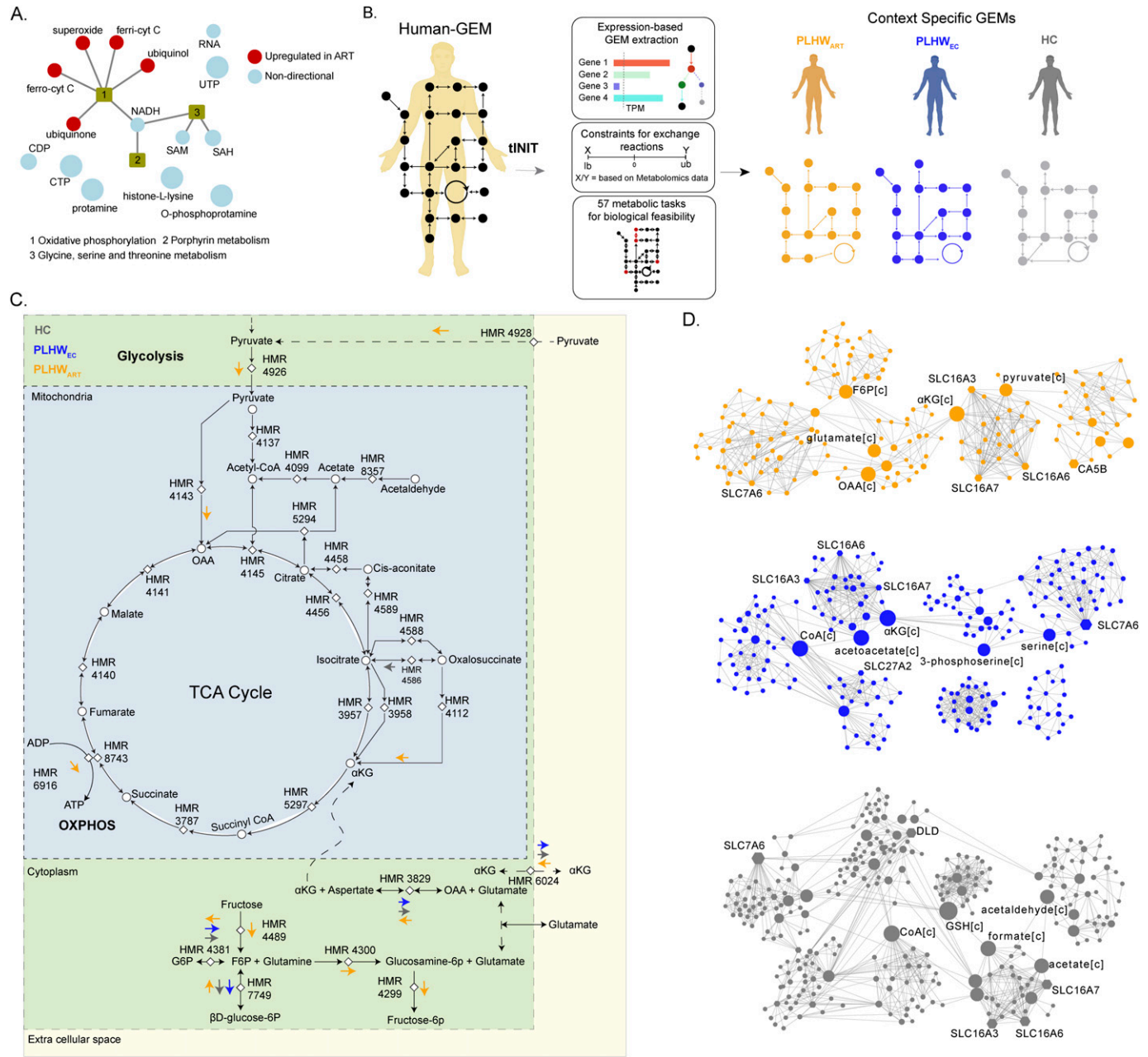


Figure 3. Context-specific genome-scale metabolic modeling and flux balance analysis.

(A) Network visualization of significant reporter metabolites (adjusted $P < 0.2$) identified in PLWH_{ART} versus PLWH_{EC}. Red-colored nodes represent up-regulated reporter metabolites and steel-blue colored nodes represent dysregulated (non-directional) reporter metabolites. (B) Workflow diagram of context-specific genome-scale metabolic model reconstruction. (C) Reaction diagram showing flux balance analysis results. Reactions show specific flux changes in PLWH_{ART} compared with PLWH_{EC} and HC cohorts highlighted with colored arrows. The direction of the arrow represents the flux change of the corresponding reaction in the cohort. (D) Communities identified from the topology analysis of the metabolic network in PLWH_{ART}, PLWH_{EC}, and HC. Node size is relative to betweenness centrality measurement. The top five ranked genes and metabolites based on betweenness centrality are labeled.

compared with PLWH_{EC} and HC cohorts. These reactions belonged to the AA, nucleotide, carbohydrate, and energy metabolism pathways. There were also 33 significant transport reactions that were transporting metabolites between cell compartments. Of the energy metabolism, pathways surrounding the tricarboxylic acid (TCA) cycle, including glycolysis, glutaminolysis, and OXPHOS, were affected in PLWH_{ART} (Fig 3C). The OXPHOS reaction converting ADP

to ATP (HMR-6916) had a positive flux in PLWH_{ART} whereas no flux was shown in PLWH_{EC} and HC, indicating that higher energy was required in PLWH_{ART}. There were also cytoplasmic reactions that appeared to increase the production of α -ketoglutarate (α KG) in PLWH_{ART}. Reactions producing fructose-6-phosphate (HMR-7749 and HMR-4489), which further feeds the reaction producing glutamate (HMR-4300), showed a positive flux in PLWH_{ART}.

whereas showing a negative or no flux in PLWH_{EC} and HC, respectively, indicative of higher glutamate production and conversion in PLWH_{ART}. The reaction converting glutamate and oxaloacetic acid (OAA) to α KG and aspartate (HMR-3829) also showed a flux towards α KG production in PLWH_{ART} and the opposite direction in PLWH_{EC} and HC. Also, the transporter reaction (HMR-6024) transporting α KG from extracellular space to the cytoplasm showed a flux in PLWH_{ART}. The reactions mentioned above signify increased accumulation of α KG in the cytoplasm in PLWH_{ART} that can feed the TCA cycle in the mitochondria. The reaction producing OAA from pyruvate (HMR-4143) and the reaction producing α KG from oxalosuccinate (HMR-4112) had positive flux in PLWH_{ART} indicating activation of the TCA cycle. To further understand the metabolic rearrangements, we performed a topological analysis on metabolic networks generated for PLWH_{ART}, PLWH_{EC}, and HC cohorts. The metabolic networks were generated by drawing edges between reactants, products, and associated genes of the reactions found to exhibit significant ($>10^{-5}$ mmol/h/gDCW) and diverging flux among the three cohorts. Communities were identified and betweenness centrality of the nodes was calculated to rank the genes and metabolites for their influence in the network. The top five metabolites and genes in PLWH_{ART}, PLWH_{EC}, and HC based on node centrality measurements are shown in Fig 3D. The metabolites fructose-6-phosphate, OAA, glutamate, and pyruvate uniquely play a central role in PLWH_{ART} indicative of a role of TCA cycle and glycolysis in differentiating PLWH_{ART} from PLWH_{EC} and HC. Transporter genes of the SLC16 gene family (monocarboxylate transporters) SLC16A3, SLC16A6, and SLC16A7 were central in all three groups further suggesting a role for pyruvate and lactate transport. Combining these results, it can be concluded that reactions surrounding the TCA cycle including glutaminolysis, OXPHOS, and glycolysis differentiate PLWH_{ART} from PLWH_{EC} and HC.

Long-term cART disrupts redox homeostasis in the lymphocytic cell population

The earlier used antiretrovirals frequently induced severe adverse effects that were linked to the occurrence of oxidative stress and mitochondrial damage (Smith et al, 2017). As we observed an up-regulation of superoxide, ubiquinol, ubiquinone, ferricytochrome C, and ferrocyanochrome C in PLWH_{ART} we evaluated total cellular ROS levels in different PBMCs subpopulations from PLWH_{ART} (n = 16), PLWH_{EC} (n = 16), and HC (n = 18), using flow cytometry (Fig S3A). The distribution of CD4⁺ and CD8⁺ T cells, classical (CM), intermediate (IM), and non-classical monocytic (NCM) populations are depicted in UMAP (Fig 4A). The percentage of CD4⁺ T cells were decreased, whereas CD8⁺ T cells were increased in PLWH_{EC} and PLWH_{ART} compared with HC (Fig S3B). PLWH_{EC} also exhibited a decreased proportion of CM compared with HC, but no other differences were identified on the monocytic subpopulations (Fig S3C). We did not observe any significant differences in ROS on CD4⁺ or CD8⁺ T cells (Figs 4B and S3D). In CM, ROS was significantly higher in PLWH_{ART} samples compared with HC (Fig 4B). Some of the PLWH_{ART} had higher ROS, whereas others expressed lower ROS on lymphocytic cell populations (Fig 4C). Therefore, to determine if long-term successfully treated HIV-1 infection influenced ROS production, we divided arbitrarily the PLWH_{ART} group into long-term ART (>10 yr,

n = 8] with a median of 19 [16–22] yr treatment) and short-term cART (<10 yr, n = 8] with a median of 7 [6–8] yr treatment). Interestingly, levels of ROS were increased in long-term ART compared with short-term ART on CD4⁺ T cells and compared with short-term ART and PLWH_{EC} on CD8⁺ T cells (Fig 4D). ROS levels were not affected by cART treatment on the monocytic cell populations (Fig S3E). These data highlights the effects of long-term cART treatment on oxidative stress and redox homeostasis in lymphocytic cell populations.

Pharmacological inhibition of OXPHOS influences latency reversal and immunosenescence in an HIV latent lymphocytic cell model

In the ex vivo part of this study, we showed how up-regulation of OXPHOS was a signature of PLWH_{ART} that differentiated them from the PLWH_{EC} and how long-term treatment influenced oxidative stress and redox homeostasis on lymphocytic cell populations. Therefore, we decided to study the effect of inhibiting OXPHOS complexes I–V in a lymphocytic latency cell model (J-Lat 10.6) together with the parental cell line (Jurkat) by targeting complex I (metformin), complex II (D- α -tocopheryl succinate, α TOS), complex III (antimycin), complex IV (arsenic trioxide), and complex V (oligomycin) (Fig 5A) with respect to apoptotic properties, latency reversal and cellular senescence. The drugs did not have any effect on cell viability (Figs 5B and S4A), although inhibition of complex I, III, and IV in J-Lat 10.6 increased the levels of Annexin V (a marker of apoptosis) compared with the respective untreated control, whereas only inhibition of complex I and IV showed the same effect in Jurkat cells (Figs 5C and S4B). This indicates the role of OXPHOS complex III in the apoptotic properties of the HIV-1 latent cell model. It was only when inhibiting complex IV a significant increase in HIV-1 reactivation was observed in J-Lat 10.6 cells (Figs 5D and S4C). Several studies including ours have shown that PLWH_{ART} has a potential for attenuated immune aging due to a shift in glutaminolysis, in a subset of PLWH_{ART} who had dysregulated metabolic profiles. A recent pivotal study also indicated a role of glutaminolysis in senolysis (removal of senescence cells) as senescent cells are dependent on glutaminolysis (Johmura et al, 2021). To prove this, we measured the senescence markers CD57, Ki-67, and PCNA using flow cytometry and DNA damage marker H2AX (S139) by Western blot. Cell surface expression of CD57 was not altered compared with the respective control when inhibiting the OXPHOS complexes although a baseline increase in CD57 was seen in J-Lat 10.6 cell compared with Jurkat (Fig S5A–C). The proportion of Ki-67-negative J-Lat 10.6 cells increased after inhibiting complexes II, III, and IV, whereas only inhibition of complex IV increased the proportion of Ki-67 negative Jurkat cells (Figs 5E and S5D). A mild decrease in Ki-67 negative cells was also observed in J-Lat 10.6 cells when inhibiting complex I (Figs 5E and S5D). Inhibition of complex III increased PCNA negative J-Lat 10.6, whereas no significant differences were observed in Jurkat cells (Figs 5F and S5E). Furthermore, phosphorylation of H2AX (S139) increased when inhibiting complex IV and decreased when inhibiting complex I, irrespective of the cell type (Figs 5G and H and S5F). The original blots were presented as a source file to Fig 5. Collectively, our data highlighted the potential role of pharmacological inhibition of the OXPHOS complexes with differential regulation of latency reversal, apoptotic properties, and

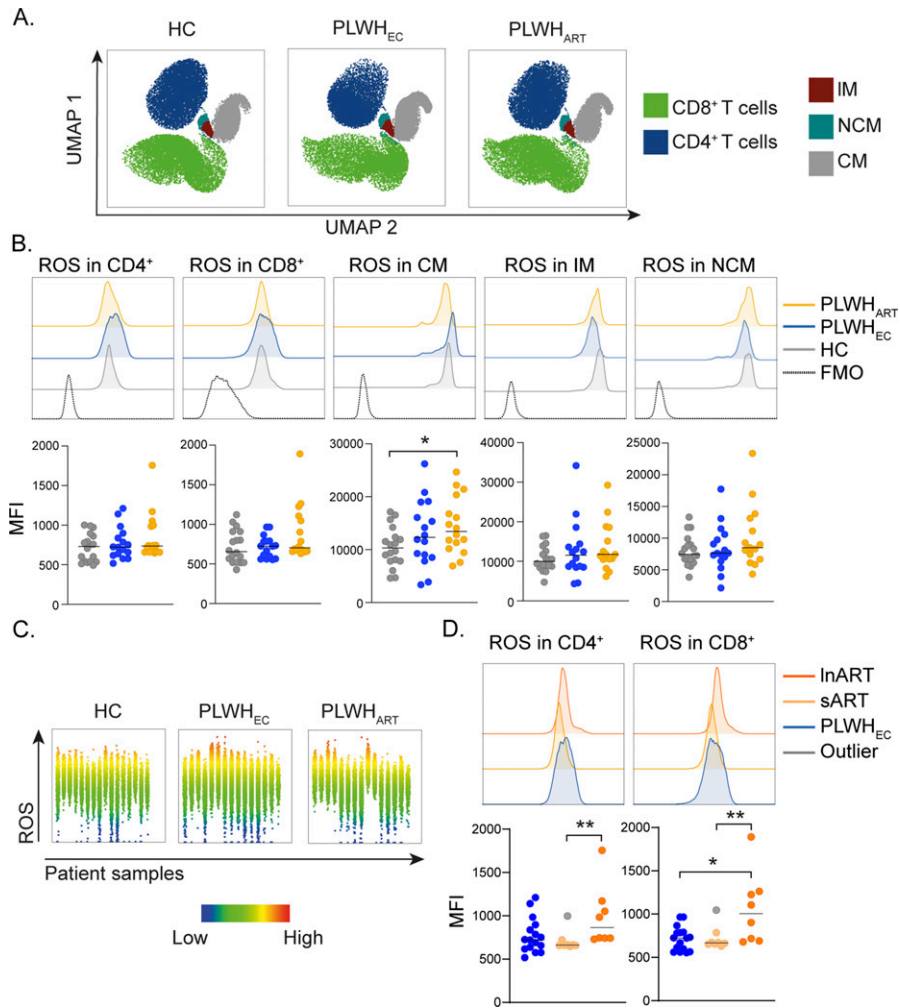


Figure 4. Redox homeostasis during suppressive viremia.

(A) Reactive oxygen species (ROS) detection in lymphocytic and monocytic cell populations from HC (n = 18), PLWH_{EC} (n = 16), and PLWH_{ART} (n = 18). UMAP representation showing the distribution of lymphocytic (CD4⁺ and CD8⁺ T cells) and monocytic (classical monocytes [CM], intermediate monocytes [IM], and non-classical monocytes [NCM]) cell populations. (B) Median fluorescence intensity (MFI) of ROS in CD4⁺, CD8⁺, CM, IM, and NCM in the cohort. Histograms show a representative sample from HC, PLWH_{EC}, and PLWH_{ART} exhibiting the median expression in each group. (C) Graphs showing MFI of ROS in each individual from HC, PLWH_{EC}, and PLWH_{ART}. (D) MFI of ROS in PLWH_{EC} (n = 16), short-term ART (sART, n = 8), and long-term ART (InART, n = 8). Histograms show a representative sample from PLWH_{EC}, sART, and InART exhibiting the median expression in each group. Statistical significance was determined using Mann–Whitney U test (P < 0.05 with * < 0.05, ** < 0.03, *** < 0.002) and represented with median. See also Fig S3.

cellular senescence in lymphocytic HIV-1 latent cell model, depending on compounds and targeted complexes.

Discussion

In the present study, we combined system-level blood cell transcriptomics and developed context-specific GSMM to provide a comprehensive system-level characterization of HIV-1 infected individuals with suppressive viremia either by natural (PLWH_{EC}) or drug-induced (PLWH_{ART}) control. The transcriptomic data identified up-regulation of OXPHOS as the characteristic feature of PLWH_{ART}, differentiating them from HIV-1 seropositive PLWH_{EC}, who were not on therapy. The main dysregulation seemed to occur in complexes I, III, and IV of the OXPHOS pathway. FBA identified altered flux in several glycolytic intermediates like pyruvate, αKG, glutamate, and fructose-6-phosphate in PLWH_{ART} compared with PLWH_{EC} and HC. Long-term cART also affected the redox homeostasis in T lymphocytes. The in vitro pharmacological inhibition of the OXPHOS complexes in the latent lymphocytic cell model suggested a role of the complex IV in latency reversal, complex I, III, and IV in apoptosis, and complex IV in immunosenescence.

Disrupted AA and central carbon metabolism have been proposed as a prominent characteristic of PLWH on long-term successful cART as reported by us and others (Mukerji et al, 2016; Babu et al, 2019; Rosado-Sánchez et al, 2019; Valle-Casuso et al, 2019; Gelpi et al, 2021; Meeder et al, 2021; Shytaj et al, 2021; Villumsen et al, 2022). Altered glutaminolysis (i.e., glutamine lysed to glutamate) and increased plasma glutamate have been observed in several cohorts from both high income (Gelpi et al, 2021) and low- and middle-income countries (Gelpi et al, 2021) and are required for optimal HIV-1 infection of CD4⁺ T cells (Clerc et al, 2019). Glutaminolysis is the primary pathway fueling the TCA cycle and OXPHOS in naïve and memory T cell subsets which are critical factors for immune recovery in successfully treated PLWH (Rosado-Sánchez et al, 2019). HIV-1 infection is more common in T cells with elevated glycolysis and OXPHOS and inhibition of these metabolic activities can block HIV-1 replication and reservoir transactivation (Valle-Casuso et al, 2019). Impairment of the metabolic steps preceding OXPHOS can also result in lipid accumulation in macrophages (Castellano et al, 2019). Enhanced glycolysis and OXPHOS are characteristics of CD8⁺ T cell exhaustion (Rahman et al, 2021). However, long-term molecular immune pathogenic consequences of successful cART have not yet been evaluated. In our study, we identified system-level

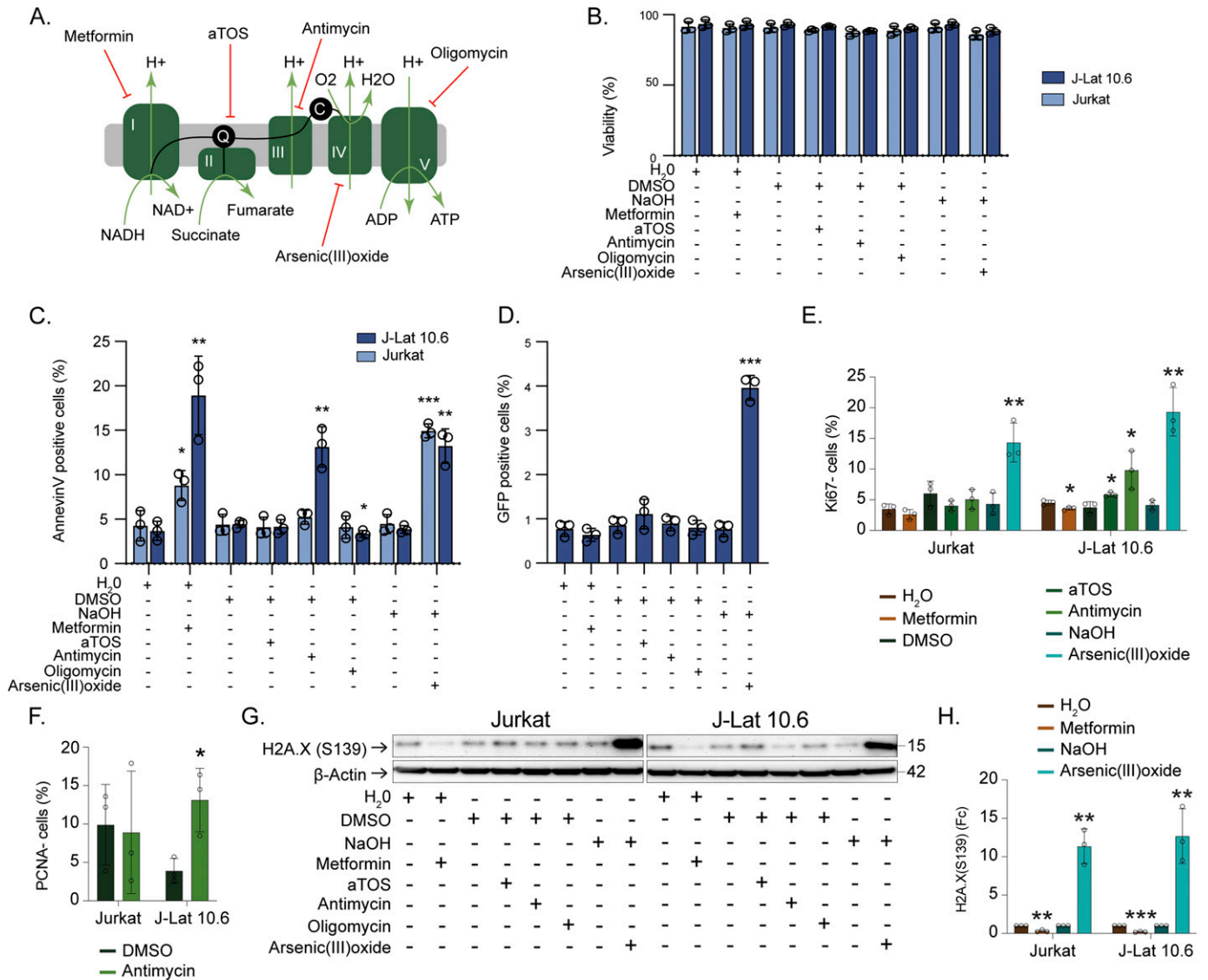


Figure 5. Pharmacological inhibition of OXPHOS in lymphocytic HIV-1 latency cell model.

(A) Schematic representation of inhibition of OXPHOS complexes with metformin (complex I), aTOS (complex II), antimycin (complex III), arsenic trioxide (complex IV), and oligomycin (complex V). (B) Drug toxicity for 24 h treatment of OXPHOS inhibitors. (C) Annexin V positive cells after treatment with OXPHOS inhibitors and respective controls. (D) Activation from latency in J-Lat 10.6 cells after treatment with OXPHOS inhibitors and respective controls. (E) Percentage Ki-67 negative cells after treatment with OXPHOS inhibitors or respective controls. (F) Percentage PCNA negative cells after treating with Antimycin or DMSO control. (G) Western blot detection of H2A.X (S139) and β -Actin in Jurkat and J-Lat 10.6 after treatment with OXPHOS inhibitors or respective controls. (H) Quantification of H2A.X (S139). The graph shows fold change (Fc) of protein expression in relation to respective control after normalization to β -Actin. Experiments were performed in three biological replicates. Significance was determined using two-tailed t test ($P < 0.05$ with * < 0.05 , ** < 0.033 , *** < 0.002) and represented with mean and SD. Significance for each drug is compared with respective control. See also Figs S4 and S5. Source data are available online for this figure.

up-regulation of OXPHOS as the main characteristic of PLWH on long-term cART. When comparing with PLWH_{EC}, an up-regulation of OXPHOS, and to certain extent glycolysis, was observed in PLWH_{ART}. Given that HIV-1 preferentially selects cells that have elevated cellular OXPHOS and glycolysis for infection and replication, reservoir seeding (Hegedus et al, 2014; Palmer et al, 2014; Valle-Casuso et al, 2019) and cell-to-cell spread of HIV-1, this metabolic environment permit ongoing replication during cART (Sigal et al, 2011). Therefore, we hypothesize that up-regulation of OXPHOS in PLWH_{ART} was the reason behind the relatively larger HIV-1 reservoir

in long-term successfully treated infection compared with PLWH_{EC} with natural control of viral replication. This metabolic modulation could potentially be a barrier to the post-treatment control of viral replication.

A recent seminal study showed that a higher HIV-1 viral set point in untreated patients during acute HIV-1 infection correlated positively with OXPHOS and that in vitro pharmacological inhibition of complex I (by rotenone or metformin) and complex III (by antimycin A) suppressed viral replication and immunometabolism through an NLRX1 and FASTKD5-dependent mechanism (Guo et al,

2021). Furthermore, we recently observed that blocking glycolysis with 2-deoxyglucose (2-DG) increased cell death in lymphocytic and pre-monocytic HIV-1 latent cell models (Gelpi et al, 2021), in line with other studies (Valle-Casuso et al, 2019; Guo et al, 2021). These studies indicate a critical role for glycolysis and OXPHOS in HIV-1 immuno-pathogenesis. In the present study, we observed that latently infected cells treated with antimycin resulted in increased markers of apoptosis in latent J-Lat 10.6 cells compared with the parental Jurkat cells. This indicates an increased preferential cell death of the latently infected cells without latency reversal. Only inhibition of complex IV by arsenic trioxide showed a small degree of latency reversal. Both the transcriptomic data and the in vitro assays indicated the role of complex I, III, and IV as essential components of the electron transport chain for generation of ATP and cellular energy requirements. Complexes I and III have a role in ROS production and are essential in inflammatory macrophages and T helper 17 (T_H17) cells while also playing a vital role in lymphocyte activation, proliferation, and differentiation (Yin & O'Neill, 2021). Recently, it has been shown that complex III is crucial for the suppressive function of Tregs (Weinberg et al, 2019). Our DCQ identified increased frequency of Tregs in PLWH_{ART} compared with PLWH_{EC} which is in line with recent findings (Caetano et al, 2020); however, PLWH_{EC} can present more activated Tregs (Gaardbo et al, 2014; Caetano et al, 2020). Finally, an earlier study reported the Cox-II enzyme leads to reduced T-cell apoptosis in HIV-1 infected cells (Tripathy & Mitra, 2010). In contrast, our study indicated pharmacological inhibition of the complex IV with arsenic trioxide increased apoptosis (as measured by the annexin V) both in latent J-Lat 10.6 cells and non-latent Jurkat. Interestingly, inhibition of complex IV in J-Lat 10.6 cells also showed latency reactivation which could potentially be linked to apoptosis.

In our FBA, we identified altered flux in pyruvate, glutamate, and α KG in the PLWH_{ART} compared with PLWH_{EC} and HC. Recently, we identified a higher level of glutamate in PLWH_{ART} in several cohorts compared with HC (Gelpi et al, 2021). The level was even higher in PLWH_{ART} with metabolic syndrome (Gelpi et al, 2021). Blood glutamate level has been reported to be higher in PLWH with dementia (Ferrarese et al, 2001). Reducing the blood glutamate concentrations with blood glutamate scavengers like pyruvate facilitates the efflux of glutamate from the brain to the blood. This can limit the neurotoxic effect of glutamate (Boyko et al, 2012) and has been reported to effectively improve neurological recovery in traumatic brain injury (Gottlieb et al, 2003; Zlotnik et al, 2007; Boyko et al, 2012). The coordination between glutamate and pyruvate and its neuroprotective role in chronic HIV-1 infected patients on therapy needs further studies to understand neurological complications in HIV infection after successful treatment.

Although immune cell senescence decreases the overall cellular activity, it is associated with a high metabolic need, usually by increasing aerobic glycolysis. In the case of our lymphocytic cell culture model, we detected an enrichment of the senescent marker CD57 compared with the parental cell line, indicative of increased chronic activation of latently infected cells. Furthermore, we detected increased levels of DNA damage (H2A.X [S139]) (Mah et al, 2010), decreased proliferation (Ki-67) (Lawless et al, 2010), and DNA replication (PCNA) (González-Magaña & Blanco, 2020) after OXPHOS inhibition. Earlier studies have shown how OXPHOS inhibition in

human fibroblasts induced senescence (Stöckl et al, 2006). Therefore, high plasticity of metabolic reprogramming could induce an increase in glycolysis during OXPHOS inhibition which could potentially be coupled to induction of senescence in the HIV-1 latent cells during the suppressive therapy.

Our study also showed that ROS was increased in patients on long-term (median 19 yr) compared with short-term (median 7 yr) of suppressive therapy. This could be linked to the use of the older nucleoside reverse transcriptase inhibitors (NRTIs) like zidovudine (AZT), stavudine (d4T), or didanosine (ddI) as a part of the initial treatment regimen. The cell's epigenetic state is closely associated with ROS-induced oxidative stress due to mitochondrial damage and altered OXPHOS (Guillaumet-Adkins et al, 2017). It is known that antiretrovirals such as AZT, d4T, and ddI can cause mitochondrial damage, ultimately altering OXPHOS (Pinti et al, 2006). Recent molecular studies have reported that PLWH on treatment has epigenetic age acceleration (Gross et al, 2016) compared with the non-infected individuals that can partially be reversed with cART initiation (Esteban-Cantos et al, 2021). Therefore, understanding the biological mechanism of potential accentuated aging in PLWH on long-term successful therapy who were exposed to earlier generation treatment regimen and dysregulated metabolic profile could potentially provide a clinical intervention strategy to improve the quality of life of PLWH_{ART}.

In conclusion, our study indicated a system-level up-regulation of OXPHOS and, to a certain extent, glycolysis in PLWH_{ART} compared with the PLWH_{EC}. Furthermore, we show how this up-regulation could play a role in latent reservoir dynamics and immunosenescence in HIV-1-infected individuals with long-term successful therapy. Pharmacological inhibition of the OXPHOS complexes could have a role in latency reversal, apoptotic properties, and immunosenescence in latently infected cells. Further studies are warranted to elucidate the molecular mechanisms underlying the observed shift in OXPHOS in PLWH_{ART} and how its coordination with glutaminolysis can lead to immune dysregulation during successful therapy.

Materials and Methods

Cohort description

The study population includes three groups of PLWH, with two groups as suppressed viremia (PLWH_{ART} and PLWH_{EC}, n = 19 each), and one group with viremia (PLWH_{VP} herein, n = 19). In addition, we enrolled 19 HC. The study was approved by the regional ethics committees of Stockholm (2013/1944-31/4 and 2009/1485-31) and amendment (2019-05585 and 2019-05584, respectively) and performed in accordance with the Declaration of Helsinki. All participants gave informed consent. The patient's identity was anonymized and delinked before analysis.

Transcriptomics analysis

PBMCs were used for RNA-sequencing (RNA-Seq) using Illumina HiSeq2500 or NovaSeq6000 as described by us (Akusjärvi et al, 2022). Differential gene expression analysis was performed using

the R/Bioconductor package DESeq2 v1.26.0 (DOI: [10.18129/B9.bioc.DESeq2](https://doi.org/10.18129/B9.bioc.DESeq2)). Gene list enrichment analysis for cART-specific genes was performed using enrichr module of python package GSEAPY v0.9.16 (Subramanian et al, 2005; Chen et al, 2013) and MSigDB hallmark gene set v7.4. GSEA between PLWH_{ART} and PLWH_{EC} was performed using GSEA v4.1.0 software (Subramanian et al, 2005) and MSigDB hallmark gene set v7.4. Metabolomics data were generated using the Metabolon HD4 (Metabolon Inc.) (Akusjärvi et al, 2022).

DCQ

DCQ by measuring the proportion of different cells in each sample was performed using the deconvolution algorithm adapted from Estimating the Proportions of Immune and Cancer cells (Chen et al, 2013). The reference gene expression profile consists of gene-level expression data of 18 blood cell types and it is based on Human Protein Atlas version 20.1 and Ensembl version 92.38. Signature genes for the 18 blood cell types in the reference profile were downloaded from CellMarker (Zhang et al, 2019) and PanglaoDB (Franzén et al, 2019). The transcript per million (TPM) transformed gene expression data of all genes from the samples were used in the procedure along with reference profile and signature gene list to estimate the cell proportion.

ART-specific gene identification

Significantly regulated genes (adjusted $P < 0.05$) in all the pair-wise comparisons among the four cohorts were used to derive the cART-specific genes. The list of significant genes in each of the comparisons was considered as individual sets and various set operation procedures were used for the derivation. The set operations performed are represented below.

$$\begin{aligned} \text{ART} &= \{z \mid z \in X_1 \text{ or } z \in X_2 \text{ or } z \in X_3\} \\ \text{NULL} &= \{z \mid z \in Y_1 \text{ or } z \in Y_2 \text{ or } z \in Y_3\} \\ \text{ART-specific genes} &= \{z \mid z \in \text{ART} \text{ and } z \notin \text{NULL}\} \end{aligned}$$

where,

$$\begin{aligned} X_1 &= \{z \mid z \text{ is gene regulated in HC versus PLWH}_{\text{ART}}\} \\ X_2 &= \{z \mid z \text{ is gene regulated in PLWH}_{\text{EC}} \text{ versus PLWH}_{\text{ART}}\} \\ X_3 &= \{z \mid z \text{ is gene regulated in PLWH}_{\text{VP}} \text{ versus PLWH}_{\text{ART}}\} \\ Y_1 &= \{z \mid z \text{ is gene regulated in HC versus PLWH}_{\text{VP}}\} \\ Y_2 &= \{z \mid z \text{ is gene regulated in PLWH}_{\text{EC}} \text{ versus PLWH}_{\text{VP}}\} \\ Y_3 &= \{z \mid z \text{ is gene regulated in HC versus PLWH}_{\text{EC}}\} \end{aligned}$$

GSMM, FBA, and essentiality analysis

Group-specific human GSMMs were reconstructed by integrating transcriptomics data on human reference GSMM obtained from Metabolic Atlas (Robinson et al, 2020). The metabolic model reconstruction was performed using task-driven Integrative Network Inference for Tissues (tINIT) algorithm (Agren et al, 2012, 2014; Robinson et al, 2020). The algorithm creates a context-specific model by selecting only reaction that can carry flux based on the provided transcript expression table (transcript per million). The

reconstructed models were then checked for biological feasibility by analyzing their capacity to carry out 56 essential metabolic tasks. FBA was performed using MatLab function solveLP from RAVEN toolbox v2.4.0 (Wang et al, 2018) and ATP hydrolysis as objective function. Plasma metabolomics data were used as a reference to constrain the exchange reactions in the model assuming that exchange reaction fluxes were relatively influenced by availability of extracellular metabolites. We calculated \log_2 -scaled changes of exchange metabolites against the control cohort, and it was used proportionally to compute the reaction bounds.

Network topology analysis was performed on the metabolic networks generated for the cohorts. The metabolic networks were created by drawing edges between reactants, products, and enzymatic genes of each of the reactions, which showed significant ($>10^{-5}$) and varying flux values among the cohorts. The networks were then analyzed using igraph toolkit. The absolute value of the flux scaled between 0 and 1 was used as edge weight. Leiden algorithm (Traag et al, 2019) was used to identify communities and the betweenness centrality of all the nodes was computed. Nodes were ranked based on their centrality measurement. Nodes with high centrality were considered as most influential for the existence and functioning of the network.

Visualization

R package ggplot2 v3.3.2 (Wickham, 2016) was used to create all bubble plots, scatter plots, and boxplots. R/Bioconductor package ComplexHeatmap v2.2.0 (Gu et al, 2016) was used to create all the heat maps. Network diagrams were drawn in Cytoscape ver 3.6.1 (Shannon et al, 2003). Venn diagrams were generated using the online tool InteractiVenn (Chen & Boutros, 2011).

Total HIV DNA quantification

Total DNA was extracted from PBMCs using QIAamp DNA mini kit (QIAGEN) according to manufacturers' instructions. HIV-1 DNA quantification was performed using Internally Controlled qPCR (IC-qPCR) as described by Vicenti et al (2018). In brief, total HIV-1 DNA was quantified in PLWH_{ART} ($n = 17$) and PLWH_{EC} ($n = 14$) using 500 ng of DNA in duplicates. Quantification was performed using Takara Universal Mastermix (Takara) on an ABI 7500F using primers (β globin F; AGGGCCTCACCACCAACTT, β globin R; GCACCTGACTCTGAGGAGAA, HXB2 F; GCCTCAATAAAGCTTGCCTTGA, HXB2 R; GGCGCCACTGCTAGAGATTTT) and probes (β globin; HEX-ATCCACGTTACCTTGCCCCACATAM, HXB2; FAM-AAGTAGTGTGCCCCGCTG-MGBEQ) targeting β globin and HIV-1 (HXB2) and normalized to β globin levels.

Cell culture

The latency cell model J-Lat clone 10.6 (NIH HIV reagent program) was used together with its parental cell line Jurkat. Cells were cultured in StableCell RPMI 1640 (Sigma-Aldrich) supplemented with 10% fetal bovine serum (Gibco) and 20 U/ml penicillin and 20 $\mu\text{g/ml}$ streptomycin (Gibco) at 37°C and 5% CO_2 .

Drug treatment

Cytotoxicity assays were performed for metformin (Sigma-Aldrich), arsenic trioxide (Sigma-Aldrich), oligomycin (Sigma-Aldrich), anti-mycin (Sigma-Aldrich), and aTOS (Sigma-Aldrich) (Fig S3A). Experimental concentrations with low cytotoxicity were chosen and assayed for 24 h. All assays were performed in biological triplicates and analyzed for viability using flow cytometry, as described below.

Flow cytometry

PBMCs were subjected to flow cytometry analysis. Samples were thawed in 37°C water bath and washed with flow cytometry buffer (PBS + 2% FBS + 2 mM EDTA). Total cellular ROS levels were measured using the CellROX Deep Red Flow Cytometry Assay Kit (Invitrogen) according to the manufacturer's instructions. Briefly, 750 nM of CellROX deep red reagent was added to PBMCs and incubated for 1 h at 37°C, protected from light. The cells were then stained with Live/Dead fixable near-IR dye (Invitrogen), and cell surface markers were detected by incubating cells with anti-CD3 (clone OKT3, BD Bioscience), anti-CD4 (clone SK3; BD Bioscience), anti-CD8 (clone HIT8a; BioLegend), anti-CD14 (clone M5E2; BioLegend), and anti-CD16 (clone 3G8; BD Bioscience) for 20 min on ice in flow cytometry buffer. Positive and negative controls for ROS measurement were performed by incubating cells with either tert-butyl hydroperoxide (200 μ M) or N-acetyl cysteine (5 mM) for 45 min at 37°C before the addition of CellROX deep red reagent. All cells were fixed with 2% paraformaldehyde before acquiring on BD FACS Symphony flow cytometer (BD Bioscience). Compensation setup was performed using single-stained controls prepared with antibody-capture beads: anti-mouse Ig, κ /negative control compensation particles set (BD Biosciences) for mouse antibodies and ArC amine-reactive compensation bead kit (Invitrogen) for use with LIVE/DEAD fixable dead cell stain kits.

Flow cytometry for cell lines was conducted by extracellular staining using anti-CD57 (clone HNK-1; BioLegend) and LIVE/DEAD Near-IR viability stain (Invitrogen) followed by fixation using ki-67 fixation/permeabilization kit (eBioscience). Intracellular staining was performed using anti-Ki-67 (clone Ki-67; BioLegend) and anti-PCNA (clone PC10; BioLegend). Analysis of apoptosis was performed using Annexin-V Alexa647 conjugate (Thermo Fisher Scientific) staining in combination with LIVE/DEAD Near-IR viability stain (Invitrogen) prior fixation using 4% PFA. Samples were acquired on BD FACS Fortessa (BD Bioscience). Flow cytometry data were analyzed and compensated with FlowJo 10.6.2 (TreeStar Inc.) and statistical analysis was performed using Mann-Whitney *U* test or two-tailed *t* test in Prism 9.3.0 (GraphPad Software Inc.).

Western blot

Cells were lysed in RIPA buffer (Sigma-Aldrich) supplemented with 1 \times PhosSTOP (Sigma-Aldrich) and 2 \times cOMplete protease inhibitor cocktail (Roche) on ice for 30 min. Protein estimation was performed using DC protein assay (Bio-Rad Laboratories) and 37.5–48 μ L of protein run in each well on NuPage 4–12% BisTris 20 well, 1 mm precast gels (Thermo Fisher Scientific) and transferred using the iBlot transfer system (Invitrogen) with iBlot PVDF Transfer stack

(Invitrogen). Membranes were incubated with Phospho-Histone H2A.X (Ser139) (Cell Signaling Technology) and β -Actin (Sigma-Aldrich). Secondary antibody incubation was performed using Dako Immunoglobulins/HRP (Aglient Technologies) and membranes developed using ECL (Amersham) on ChemiDoc (Bio-Rad Laboratories). Relative protein quantification was performed using ImageLab 6.0.1 (Bio-Rad Laboratories) and statistical significance using a two-tailed *t* test in Prism 9.3.0 (GraphPad Software Inc.).

Data Availability

The raw RNA sequencing (RNAseq) data have been deposited in the NCBI/SRA with PRJNA420459. The metabolomics data are available from [dx.doi.org/10.6084/m9.figshare.19747582](https://doi.org/10.6084/m9.figshare.19747582). All the codes are available at github: github.com/neogilab/LongART.

Supplementary Information

Supplementary Information is available at <https://doi.org/10.26508/lsa.202201405>.

Acknowledgements

The authors acknowledge support from the National Genomics Infrastructure in Genomics Production Stockholm funded by Science for Life Laboratory, the Knut and Alice Wallenberg Foundation and the Swedish Research Council, and SNIC/Uppsala Multidisciplinary Center for Advanced Computational Science for assistance with massively parallel sequencing and access to the UPPMAX computational infrastructure. The study is funded by the Swedish Research Council grants 2017-01330, 2018-06156, and 2021-01756 to U Neogi and 2017-05848 and 2020-02129 to A Sönnernborg.

Author Contributions

AT Ambikan: data curation, formal analysis, investigation, visualization, methodology, and writing—original draft.
S Svensson-Akusjärvi: data curation, formal analysis, visualization, methodology, and writing—original draft.
S Krishnan: visualization, methodology, and writing—review and editing.
M Sperk: formal analysis, methodology, and writing—review and editing.
P Nowak: data curation, investigation, and writing—review and editing.
J Vesterbacka: data curation, investigation, and writing—review and editing.
A Sönnernborg: conceptualization, resources, funding acquisition, investigation, project administration, and writing—review and editing.
R Benfeitas: supervision, visualization, methodology, project administration, and writing—review and editing.
U Neogi: conceptualization, resources, supervision, funding acquisition, visualization, methodology, writing—original draft and project administration.

Conflict of Interest Statement

The authors declare that they have no conflict of interest.

References

- Agren R, Bordel S, Mardinoglu A, Pornputtpong N, Nookaew I, Nielsen J (2012) Reconstruction of genome-scale active metabolic networks for 69 human cell types and 16 cancer types using INIT. *PLoS Comput Biol* 8: e1002518. doi:10.1371/journal.pcbi.1002518
- Agren R, Mardinoglu A, Asplund A, Kampf C, Uhlen M, Nielsen J (2014) Identification of anticancer drugs for hepatocellular carcinoma through personalized genome-scale metabolic modeling. *Mol Syst Biol* 10: 721. doi:10.1002/msb.145122
- Akusjärvi SS, Ambikan AT, Krishnan S, Gupta S, Sperk M, Végvári Á, Mikaeloff F, Healy K, Vesterbacka J, Nowak P, et al (2022) Integrative proteo-transcriptomic and immunophenotyping signatures of HIV-1 Elite control phenotype: A cross-talk between glycolysis and HIF signaling. *iScience* 25: 103607. doi:10.1016/j.isci.2021.103607
- Ambikan AT, Yang H, Krishnan S, Svensson-Akusjärvi S, Gupta S, Lourda M, Sperk M, Arif M, Zhang C, Nordqvist H, et al (2022) Multiomics personalized network analyses highlight progressive immune disruption of central metabolism associated with COVID-19 severity. *SSRN* doi:10.2139/ssrn.3988390
- Babu H, Sperk M, Ambikan AT, Rachel G, Viswanathan VK, Tripathy SP, Nowak P, Hanna LE, Neogi U (2019) Plasma metabolic signature and abnormalities in HIV-infected individuals on long-term successful antiretroviral therapy. *Metabolites* 9: 210. doi:10.3390/metabo9100210
- Boyko M, Melamed I, Gruenbaum BF, Gruenbaum SE, Ohayon S, Leibowitz A, Brotfain E, Shapira Y, Zlotnik A (2012) The effect of blood glutamate scavengers oxaloacetate and pyruvate on neurological outcome in a rat model of subarachnoid hemorrhage. *Neurotherapeutics* 9: 649–657. doi:10.1007/s13311-012-0129-6
- Caetano DG, de Paula HHS, Bello G, Hoagland B, Villela LM, Grinsztajn B, Veloso VG, Morgado MG, Guimarães ML, Côrtes FH (2020) HIV-1 elite controllers present a high frequency of activated regulatory T and Th17 cells. *PLoS One* 15: e0228745. doi:10.1371/journal.pone.0228745
- Cassol E, Misra V, Holman A, Kamat A, Morgello S, Gabuzda D (2013) Plasma metabolomics identifies lipid abnormalities linked to markers of inflammation, microbial translocation, and hepatic function in HIV patients receiving protease inhibitors. *BMC Infect Dis* 13: 203. doi:10.1186/1471-2334-13-203
- Castellano P, Prevedel L, Valdebenito S, Eugenin EA (2019) HIV infection and latency induce a unique metabolic signature in human macrophages. *Sci Rep* 9: 3941. doi:10.1038/s41598-019-39898-5
- Chen EY, Tan CM, Kou Y, Duan Q, Wang Z, Meirelles GV, Clark NR, Ma'ayan A (2013) Enrichr: Interactive and collaborative HTML5 gene list enrichment analysis tool. *BMC Bioinformatics* 14: 128. doi:10.1186/1471-2105-14-128
- Chen H, Boutros PC (2011) VennDiagram: A package for the generation of highly-customizable Venn and Euler diagrams in R. *BMC Bioinformatics* 12: 35–37. doi:10.1186/1471-2105-12-35
- Clerc I, Moussa DA, Vahlas Z, Tardito S, Oburoglu L, Hope TJ, Sitbon M, Dardalhon V, Mongellaz C, Taylor N (2019) Entry of glucose- and glutamine-derived carbons into the citric acid cycle supports early steps of HIV-1 infection in CD4 T cells. *Nat Metab* 1: 717–730. doi:10.1038/s42255-019-0084-1
- Esteban-Cantos A, Rodríguez-Centeno J, Barruz P, Alejos B, Saiz-Medrano G, Nevado J, Martín A, Gayá F, De Miguel R, Bernardino JJ, et al (2021) Epigenetic age acceleration changes 2 years after antiretroviral therapy initiation in adults with HIV: A substudy of the NEAT001/ANRS143 randomised trial. *Lancet HIV* 8: e197–e205. doi:10.1016/S2352-3018(21)00006-0
- Ferrarese C, Aliprandi A, Tremolizzo L, Stanzani L, De Micheli A, Dolara A, Frattola L (2001) Increased glutamate in CSF and plasma of patients with HIV dementia. *Neurology* 57: 671–675. doi:10.1212/wnl.57.4.671
- Franzén O, Gan LM, Björkegren JLM (2019) PanglaoDB: A web server for exploration of mouse and human single-cell RNA sequencing data. *Database (Oxford)* 2019: baz046. doi:10.1093/database/baz046
- Gaardbo JC, Ronit A, Hartling HJ, Gjerdrum LM, Springborg K, Ralfkiær E, Thorsteinsson K, Ullum H, Andersen AB, Nielsen SD (2014) Immunoregulatory T cells may be involved in preserving CD4 T cell counts in HIV-infected long-term nonprogressors and controllers. *J Acquir Immune Defic Syndr* 65: 10–18. doi:10.1097/QAI.0b013e3182a7c932
- Gelpi M, Mikaeloff F, Knudsen AD, Benfeitas R, Krishnan S, Svensson Akusjärvi S, Høgh J, Murray DD, Ullum H, Neogi U, et al (2021) The central role of the glutamate metabolism in long-term antiretroviral treated HIV-infected individuals with metabolic syndrome. *Aging (Albany NY)* 13: 22732–22751. doi:10.18632/aging.203622
- González-Magaña A, Blanco FJ (2020) Human PCNA structure, function and interactions. *Biomolecules* 10: 570. doi:10.3390/biom10040570
- Gottlieb M, Wang Y, Teichberg VI (2003) Blood-mediated scavenging of cerebrospinal fluid glutamate. *J Neurochem* 87: 119–126. doi:10.1046/j.1471-4159.2003.01972.x
- Gross AM, Jaeger PA, Kreisberg JF, Licon K, Jepsen KL, Khosroheidari M, Morse BM, Swindells S, Shen H, Ng CT, et al (2016) Methylome-wide analysis of chronic HIV infection reveals five-year increase in biological age and epigenetic targeting of HLA. *Mol Cell* 62: 157–168. doi:10.1016/j.molcel.2016.03.019
- Gu Z, Eils R, Schlesner M (2016) Complex heatmaps reveal patterns and correlations in multidimensional genomic data. *Bioinformatics* 32: 2847–2849. doi:10.1093/bioinformatics/btw313
- Guillaumet-Adkins A, Yañez Y, Peris-Díaz MD, Calabria I, Palanca-Ballester C, Sandoval J (2017) Epigenetics and oxidative stress in aging. *Oxid Med Cell Longev* 2017: 9175806. doi:10.1155/2017/9175806
- Guo H, Wang Q, Ghneim K, Wang L, Rampanelli E, Holley-Guthrie E, Cheng L, Garrido C, Margolis DM, Eller LA, et al (2021) Multi-omics analyses reveal that HIV-1 alters CD4⁺ T cell immunometabolism to fuel virus replication. *Nat Immunol* 22: 423–433. doi:10.1038/s41590-021-00898-1
- Hegedus A, Kavanagh Williamson M, Huthoff H (2014) HIV-1 pathogenicity and virion production are dependent on the metabolic phenotype of activated CD4⁺ T cells. *Retrovirology* 11: 98. doi:10.1186/s12977-014-0098-4
- Johmura Y, Yamanaka T, Omori S, Wang TW, Sugiura Y, Matsumoto M, Suzuki N, Kumamoto S, Yamaguchi K, Hatakeyama S, et al (2021) Senolysis by glutaminolysis inhibition ameliorates various age-associated disorders. *Science* 371: 265–270. doi:10.1126/science.abb5916
- Julg B, Dee L, Ananworanich J, Barouch DH, Bar K, Caskey M, Colby DJ, Dawson L, Dong KL, Dubé K, et al (2019) Recommendations for analytical antiretroviral treatment interruptions in HIV research trials—report of a consensus meeting. *Lancet HIV* 6: e259–e268. doi:10.1016/S2352-3018(19)30052-9
- Lawless C, Wang C, Jurk D, Merz A, von Zglinicki T, Passos JF (2010) Quantitative assessment of markers for cell senescence. *Exp Gerontol* 45: 772–778. doi:10.1016/j.exger.2010.01.018
- Mah LJ, El-Osta A, Karagiannis TC (2010) GammaH2AX as a molecular marker of aging and disease. *Epigenetics* 5: 129–136. doi:10.4161/epi.5.2.11080
- Meeder E, Matzaraki V, Vadaq N, van de Wijer L, van der Ven A, Schellekens A (2021) Unbiased metabolomics links fatty acid pathways to psychiatric symptoms in people living with HIV. *J Clin Med* 10: 5466. doi:10.3390/jcm10235466

- Mukerji SS, Locascio JJ, Misra V, Lorenz DR, Holman A, Dutta A, Penugonda S, Wolinsky SM, Gabuzda D (2016) Lipid profiles and APOE4 allele impact midlife cognitive decline in HIV-infected men on antiretroviral therapy. *Clin Infect Dis* 63: 1130–1139. doi:10.1093/cid/ciw495
- Palmer CS, Ostrowski M, Gouillou M, Tsai L, Yu D, Zhou J, Henstridge DC, Maisa A, Hearps AC, Lewin SR, et al (2014) Increased glucose metabolic activity is associated with CD4+ T-cell activation and depletion during chronic HIV infection. *AIDS* 28: 297–309. doi:10.1097/QAD.000000000000128
- Peltenburg NC, Schoeman JC, Hou J, Mora F, Harms AC, Lowe SH, Bierau J, Bakker JA, Verbon A, Hankemeier T, et al (2018) Persistent metabolic changes in HIV-infected patients during the first year of combination antiretroviral therapy. *Sci Rep* 8: 16947. doi:10.1038/s41598-018-35271-0
- Pinti M, Salomoni P, Cossarizza A (2006) Anti-HIV drugs and the mitochondria. *Biochim Biophys Acta* 1757: 700–707. doi:10.1016/j.bbabi.2006.05.001
- Racle J, Gfeller D (2020) EPIC: A tool to estimate the proportions of different cell types from bulk gene expression data. *Methods Mol Biol* 2120: 233–248. doi:10.1007/978-1-0716-0327-7_17
- Rahman AN, Liu J, Mujib S, Kidane S, Ali A, Szep S, Han C, Bonner P, Parsons M, Benko E, et al (2021) Elevated glycolysis imparts functional ability to CD8+ T cells in HIV infection. *Life Sci Alliance* 4: e202101081. doi:10.26508/lsa.202101081
- Robinson JL, Kocabaş P, Wang H, Cholley P-E, Cook D, Nilsson A, Anton M, Ferreira R, Domenzain I, Billa V, et al (2020) An atlas of human metabolism. *Sci Signal* 13: eaaz1482. doi:10.1126/scisignal.aaz1482
- Rosado-Sánchez I, Rodríguez-Gallego E, Peraire J, Viladés C, Herrero P, Fanjul F, Gutiérrez F, Bernal E, Pelazas R, Leal M, et al (2019) Glutaminolysis and lipoproteins are key factors in late immune recovery in successfully treated HIV-infected patients. *Clin Sci (Lond)* 133: 997–1010. doi:10.1042/CS20190111
- Shannon P, Markiel A, Ozier O, Baliga NS, Wang JT, Ramage D, Amin N, Schwikowski B, Ideker T (2003) Cytoscape: A software environment for integrated models of biomolecular interaction networks. *Genome Res* 13: 2498–2504. doi:10.1101/gr.1239303
- Shytaj IL, Procopio FA, Tarek M, Carlon-Andres I, Tang HY, Goldman AR, Munshi M, Kumar Pal V, Forcato M, Sreeram S, et al (2021) Glycolysis downregulation is a hallmark of HIV-1 latency and sensitizes infected cells to oxidative stress. *EMBO Mol Med* 13: e13901. doi:10.15252/emmm.202013901
- Sigal A, Kim JT, Balazs AB, Dekel E, Mayo A, Milo R, Baltimore D (2011) Cell-to-cell spread of HIV permits ongoing replication despite antiretroviral therapy. *Nature* 477: 95–98. doi:10.1038/nature10347
- Smith RL, Tan JME, Jonker MJ, Jongejan A, Buissink T, Veldhuijzen S, van Kampen AHC, Brul S, van der Spek H (2017) Beyond the polymerase- γ theory: Production of ROS as a mode of NRTI-induced mitochondrial toxicity. *PLoS One* 12: e0187424. doi:10.1371/journal.pone.0187424
- Stöckl P, Hütter E, Zwerschke W, Jansen-Dürr P (2006) Sustained inhibition of oxidative phosphorylation impairs cell proliferation and induces premature senescence in human fibroblasts. *Exp Gerontol* 41: 674–682. doi:10.1016/j.exger.2006.04.009
- Subramanian A, Tamayo P, Mootha VK, Mukherjee S, Ebert BL, Gillette MA, Paulovich A, Pomeroy SL, Golub TR, Lander ES, et al (2005) Gene set enrichment analysis: A knowledge-based approach for interpreting genome-wide expression profiles. *Proc Natl Acad Sci USA* 102: 15545–15550. doi:10.1073/pnas.0506580102
- Traag VA, Waltman L, van Eck NJ (2019) From Louvain to Leiden: Guaranteeing well-connected communities. *Sci Rep* 9: 5233. doi:10.1038/s41598-019-41695-z
- Tripathy MK, Mitra D (2010) Differential modulation of mitochondrial OXPHOS system during HIV-1 induced T-cell apoptosis: Up regulation of complex-IV subunit COX-II and its possible implications. *Apoptosis* 15: 28–40. doi:10.1007/s10495-009-0408-9
- Valle-Casuso JC, Angin M, Volant S, Passaes C, Monceaux V, Mikhailova A, Bourdic K, Avettand-Fenoel V, Boufassa F, Sitbon M, et al (2019) Cellular metabolism is a major determinant of HIV-1 reservoir seeding in CD4+ T cells and offers an opportunity to tackle infection. *Cell Metab* 29: 611–626.e5. doi:10.1016/j.cmet.2018.11.015
- Vicenti I, Meini G, Saladini F, Giannini A, Boccuto A, Schiaroli E, Zazzi M (2018) Development of an internally controlled quantitative PCR to measure total cell-associated HIV-1 DNA in blood. *Clin Chem Lab Med* 56: e75–e77. doi:10.1515/cclm-2017-0587
- Villumsen SO, Benfeitas R, Dehlbæk Knudsen A, Gelpi M, Høgh J, Thomsen MT, Murray D, Ullum H, Neogi U, Nielsen SD (2022) Integrative lipidomics and metabolomics for system-level understanding of the metabolic syndrome in long-term treated HIV-infected individuals. *Front Immunol* 12: 742736. doi:10.3389/fimmu.2021.742736
- Wang H, Marcišauskas S, Sánchez BJ, Domenzain I, Hermansson D, Agren R, Nielsen J, Kerkhoven EJ (2018) RAVEN 2.0: A versatile toolbox for metabolic network reconstruction and a case study on *Streptomyces coelicolor*. *PLoS Comput Biol* 14: e1006541. doi:10.1371/journal.pcbi.1006541
- Weinberg SE, Singer BD, Steinert EM, Martinez CA, Mehta MM, Martínez-Reyes I, Gao P, Helmin KA, Abdala-Valencia H, Sena LA, et al (2019) Mitochondrial complex III is essential for suppressive function of regulatory T cells. *Nature* 565: 495–499. doi:10.1038/s41586-018-0846-z
- Wickham H (2016) *ggplot2. Elegant Graphics for Data Analysis*. New York: Springer International Publishing.
- Yang H, Arif M, Yuan M, Li X, Shong K, Türkez H, Nielsen J, Uhlén M, Borén J, Zhang C, et al (2021) A network-based approach reveals the dysregulated transcriptional regulation in non-alcoholic fatty liver disease. *iScience* 24: 103222. doi:10.1016/j.isci.2021.103222
- Yin M, O'Neill LAJ (2021) The role of the electron transport chain in immunity. *FASEB J* 35: e21974. doi:10.1096/fj.202101161R
- Zeybel M, Altay O, Arif M, Li X, Yang H, Fredolini C, Akyildiz M, Saglam B, Gonenli MG, Ural D, et al (2021) Combined metabolic activators therapy ameliorates liver fat in nonalcoholic fatty liver disease patients. *Mol Syst Biol* 17: e10459. doi:10.15252/msb.202110459
- Zhang W, Ambikan AT, Sperk M, van Domselaar R, Nowak P, Noyan K, Russom A, Sönnnerborg A, Neogi U (2018) Transcriptomics and targeted proteomics analysis to gain insights into the immune-control mechanisms of HIV-1 infected elite controllers. *EBioMedicine* 27: 40–50. doi:10.1016/j.ebiom.2017.11.031
- Zhang W, Morshed MM, Noyan K, Russom A, Sönnnerborg A, Neogi U (2017) Quantitative humoral profiling of the HIV-1 proteome in elite controllers and patients with very long-term efficient antiretroviral therapy. *Sci Rep* 7: 666. doi:10.1038/s41598-017-00759-8
- Zhang X, Lan Y, Xu J, Quan F, Zhao E, Deng C, Luo T, Xu L, Liao G, Yan M, et al (2019) CellMarker: A manually curated resource of cell markers in human and mouse. *Nucleic Acids Res* 47: D721–D728. doi:10.1093/nar/ky900
- Zlotnik A, Gurevich B, Tkachov S, Maoz I, Shapira Y, Teichberg VI (2007) Brain neuroprotection by scavenging blood glutamate. *Exp Neurol* 203: 213–220. doi:10.1016/j.expneurol.2006.08.021



License: This article is available under a Creative Commons License (Attribution 4.0 International, as described at <https://creativecommons.org/licenses/by/4.0/>).